

Mask Frozen-DETR: High Quality Instance Segmentation with One GPU

Zhanhao Liang
The Australian National University

Yuhui Yuan[†]
Microsoft Research Asia

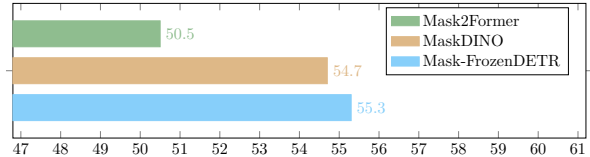
Abstract

In this paper, we aim to study how to build a strong instance segmenter with minimal training time and GPUs, as opposed to the majority of current approaches that pursue more accurate instance segmenter by building more advanced frameworks at the cost of longer training time and higher GPU requirements. To achieve this, we introduce a simple and general framework, termed *Mask Frozen-DETR*, which can convert any existing DETR-based object detection model into a powerful instance segmentation model. Our method only requires training an additional lightweight mask network that predicts instance masks within the bounding boxes given by a frozen DETR-based object detector. Remarkably, our method outperforms the state-of-the-art instance segmentation method *Mask DINO* in terms of performance on the COCO test-dev split (55.3% vs. 54.7%) while being over 10× times faster to train. Furthermore, all of our experiments can be trained using only one Tesla V100 GPU with 16 GB of memory, demonstrating the significant efficiency of our proposed framework.

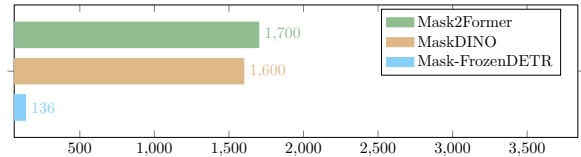
1. Introduction

Instance segmentation is one of the most fundamental but difficult computer vision tasks requiring pixel-level localization and recognition in the given input image. Most advances in modern image instance segmentation methods are heavily influenced by the latest state-of-the-art 2D object detection systems. For example, two representative leading instance segmentation approaches, including Cascade Mask R-CNN [2] and Mask DINO [18], are built by adding a parallel segmentation branch to the strong object detection systems, specifically Cascade R-CNN [1] and DINO [34].

Despite the convergence of deep neural network architectures between object detection and instance segmentation, most existing efforts still need independent training based on supervision signals of different granularity, i.e., bounding boxes vs. instance masks. Train-



(a) mask AP



(b) GPU Hours

Figure 1: Illustrating the comparison results with Mask2Former and Mask DINO on COCO instance segmentation task. (a) our Mask Frozen-DETR outperforms the previous SOTA Mask DINO by +0.5%. (b) our Mask Frozen-DETR speeds up the training by more than 10× times compared to Mask DINO.

ing modern instance segmentation models from scratch is resource-intensive and time-consuming. For example, Using ResNet-50 [15] and Swin-L [21] as backbone networks, Mask2Former [7] requires over 500× and 1700× V100 GPU hours for training, respectively.

We show that the existing DETR-based object detection models can be efficiently converted into strong instance segmentation models, unlike the previous efforts that train the instance segmentation models from scratch. We start from the recent powerful 2D object detection models, i.e., \mathcal{H} -DETR [17] and DINO-DETR [34]. We propose two key innovations: (i) design a light-weight instance segmentation network that effectively uses the output of a frozen DETR-based object detector, including the object query and the encoder feature map, to predict instance masks, and (ii) demonstrate the high training efficiency of our approach compared to the previous state-of-the-art instance segmentation approaches while achieving competitive performance under different model scales.

We conduct comprehensive comparison experiments on the COCO instance segmentation benchmark to verify the

[†]Corresponding author. ✉ yuhui.yuan@microsoft.com

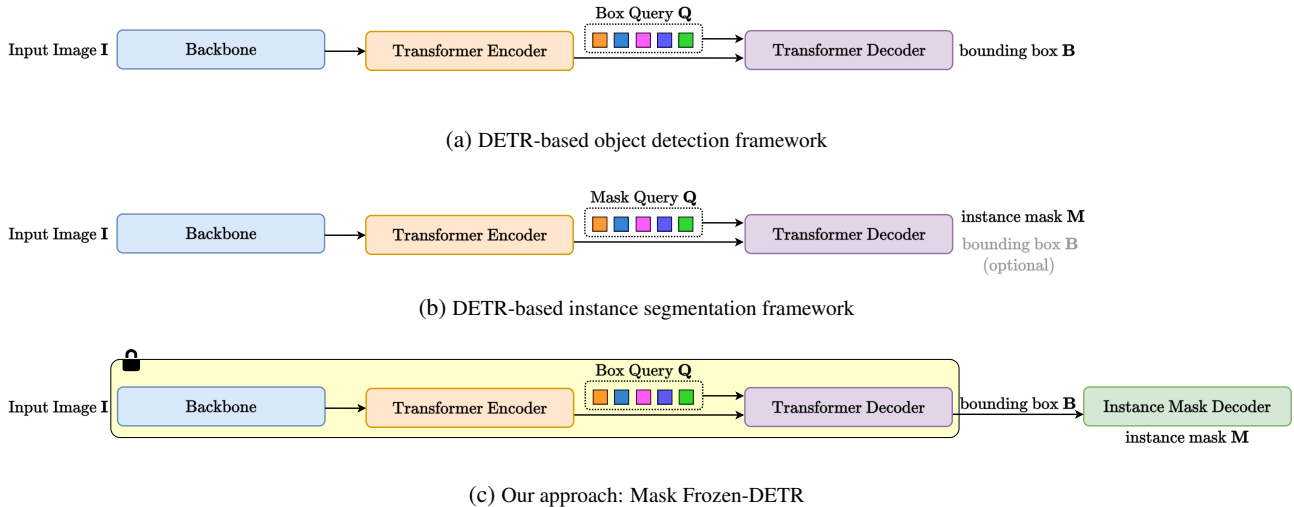


Figure 2: Illustrating the overall pipelines of DETR-based object detectors (1-st row), instance segmenters (2-ed row) based on DETR, and the proposed approach. Instead of training the instance segmentation models from scratch, we propose a Mask Frozen-DETR that uses a frozen DETR-based object detector to generate the bounding boxes and then trains a mask head to produce instance segmentation masks.

effectiveness of our approach. Our approach achieves strong results with a very short learning time. For instance, with only $6\times$ training epochs, our approach slightly surpasses the state-of-the-art method Mask DINO. Remarkably, the entire training process of our approach takes less than $140\times$ GPU hours, while Mask DINO takes nearly $1600\times$ GPU hours. Consequently, our approach improves the training efficiency by more than $10\times$. We hope our simple approach can enable broader research communities to contribute to advancing stronger instance segmentation models.

2. Related Work

Object Detection. Object detection is a fundamental research area that has produced a lot of excellent work, such as Faster R-CNN [25], Cascade R-CNN [1], YOLO [24], DETR [3], and Deformable DETR [36]. Recently, most of the exciting progress in object detection mainly comes from the developments of various DETR-based approaches, including DINO-DETR [34] and \mathcal{H} -DETR [17]. The current state-of-the-art methods [31, 20, 23, 19, 13] are also built based on them. In general, we can easily access a lot of object detection model weights based on DETR framework as most of them are open-sourced. We show our approach can be extended to these modern DETR-based detectors easily and achieves strong performance while being more than $10\times$ faster to train by exploiting the off-the-shelf pre-trained weights on object detection tasks.

Instance Segmentation. Instance segmentation is a computer vision task that requires an algorithm to assign a pixel-level or point-level mask with a category label for each in-

stance of interest in an image, video or point cloud. Most existing methods follow the R-CNN [12] paradigm, which first detects objects and then segments them. For example, Mask R-CNN [14] extends Faster R-CNN [25] with a fully convolutional mask head, Cascade Mask R-CNN combines Cascade R-CNN [1] with Mask R-CNN, and HTC [4] improves the performance with interleaved execution and mask information flow. Some recent methods propose more concise designs such as SOLO [32] that segments objects by locations without bounding boxes or embedding learning, QueryInst [11] that performs end-to-end instance segmentation based on Sparse RCNN [30], MaskFormer [9] and Mask2Former[7] that use a simple mask classification based on DETR [3], and Mask-DINO [18] that extends DINO by adding a mask prediction branch that supports all image segmentation tasks using query embeddings and pixel embeddings. Moreover, the very recent Mask3D [26] and SPFormer [29] have built state-of-the-art 3D instance segmentation systems following the design of Mask2Former.

Discussion. Most of the existing efforts train the instance segmentation models from scratch without using the off-the-shelf object detection model weights, thus requiring very expensive training. Our approach uses the weights of frozen DETR-based models and introduces a very efficient instance segmentation head design with high training efficiency. Figure 2 illustrates the differences between the existing methods and our approach. For example, the very recent state-of-the-art Mask DINO is trained from scratch while we simply freeze the existing object detector and train a very light instance mask decoder. We empirically show the great advantages of our approach on the COCO instance segmentation task with experiments under various settings.

Notably, our approach sets new records on the challenging COCO instance segmentation task while accelerating the training speed by more than $10\times$.

3. Our Approach

3.1. Baseline Setup

We use a strong object detector \mathcal{H} -DETR+ResNet50 with AP=52.2 as our baseline for the following ablation experiments and report the results based on stronger \mathcal{H} -DETR+Swin-L and DINO-DETR+FocalNet-L for the system-level comparisons. The entire \mathcal{H} -DETR+ResNet50 model is pre-trained on Object365 [27] and then fine-tuned on COCO for higher performance.

To build a simple baseline for instance segmentation without extra training, we first sort the object queries output by the last Transformer decoder layer of the object detection model according to the decreasing order of their classification scores, and select the top ~ 100 object queries for mask prediction. Then we multiply the object queries $\{\mathbf{q}_i | \mathbf{q}_i \in \mathbb{R}^d\}_{i=1}^N$ and the image features $\mathbf{F} \in \mathbb{R}^{\frac{HW}{16} \times d}$ at 1/4-resolution to get the instance segmentation masks as follows:

$$\begin{aligned} \mathbf{F} &= \mathbf{C}_1 + \text{interpolate}(\mathbf{E}), \\ \mathbf{M}_i &= \text{interpolate}(\text{reshape}(\text{Sigmoid}(\mathbf{q}_i \mathbf{F}^\top))), \end{aligned} \quad (1)$$

where $\mathbf{C}_1 \in \mathbb{R}^{\frac{HW}{16} \times d}$ represents the feature map output by the first stage of the backbone. $\mathbf{E} \in \mathbb{R}^{\frac{HW}{64} \times d}$ represents the 1/8-resolution feature map from the Transformer encoder. H , W , and d represent the image height, image width, and feature hidden dimension, respectively. $\mathbf{M}_i \in \mathbb{R}^{HW}$ represents the final predicted probability mask with the same resolution as the input image. We illustrate the overall pipeline in Figure 3.

Next, we compute the confidence scores that reflects the quality of masks following:

$$s_i = c_i \times \frac{\text{sum}(\mathbf{M}_i[\mathbf{M}_i > 0.5])}{\text{sum}([\mathbf{M}_i > 0.5])}, \quad (2)$$

where c_i represents the classification score associated with the i -th object query predicted by the last Transformer decoder layer of the object detection model.

We illustrate the modifications when using RoIAlign operation [14] as follows. Instead of using the entire image features $\mathbf{F} \in \mathbb{R}^{\frac{HW}{16} \times d}$, we use the RoIAlign to gather the region feature maps located within the predicted bounding boxes:

$$\mathbf{R}_i = \text{reshape}(\text{RoIAlign}(\text{reshape}(\mathbf{F}), \mathbf{b}_i)), \quad (3)$$

where $\mathbf{R}_i \in \mathbb{R}^{hw \times d}$, \mathbf{b}_i represents the predicted bounding box of \mathbf{q}_i . We set h and w as 32 by default. Then we com-

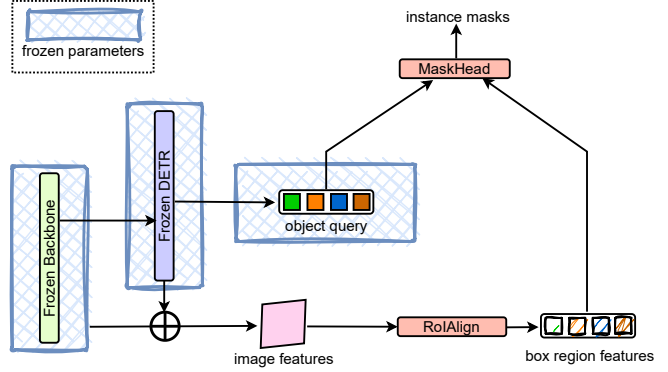


Figure 3: Mask Frozen-DETR Baseline: both RoIAlign and MaskHead are non-parametric operations.

RoIAlign	1/4 feat.	#FLOPs▲	#params▲	AP _{mask}	AP _{mask} ₅₀	AP _{mask} ₇₅	AP _{mask} _S	AP _{mask} _M	AP _{mask} _L
✗	✗	1.49 G	0.0 M	0.0	0.1	0.0	0.0	0.0	0.1
✓	✗	0.53 G	0.0 M	4.4	14.8	1.3	2.7	4.6	7.5
✗	✓	1.50 G	0.0 M	0.0	0.1	0.0	0.0	0.0	0.1
✓	✓	0.54 G	0.0 M	5.1	17.0	1.5	3.2	4.9	8.4

Table 1: **Effect of each factor within our baseline that requires no training.** RoIAlign: use RoIAlign to pool the region features according to the predicted boxes. 1/4 feat.: fuse the 1/4-resolution feature maps output by the stage-1 of backbone with the up-sampled 1/4-resolution feature maps output by the Transformer encoder. We use ▲ to mark the additional increased number of parameters and FLOPs in all the following tables.

pute the instance segmentation masks as follows:

$$\mathbf{M}_i^r = \text{paste}(\text{interpolate}(\text{reshape}(\text{Sigmoid}(\mathbf{q}_i \mathbf{R}_i^\top)))), \quad (4)$$

where we first reshape and interpolate the predicted regional instance masks to be the same size as the real bounding box size in the original image and then paste the resized ones to an empty instance mask of the same size as the original image. We compute the confidence scores based on \mathbf{M}_i^r following a similar manner.

Results. Table 1 shows the comparison results on the effect of fusing the 1/4-resolution feature maps output by the first stage of the backbone and using the RoIAlign to constrain the computation focus only within the predicted bounding boxes. According to the reported results, we find that directly multiplying the object queries with the image feature maps performs very poorly, i.e., the best setting achieves a mask AP score 5.1%. Notably, we also report the additional increased computational cost and number of parameters in all ablation experiments by default.

We aim to make minimal modifications to boost the segmentation performance based on the above baseline setting. We show how to improve the system from three main aspects, including image feature encoder design, box region feature encoder design, and query feature encoder design,



Figure 4: Coarse instance segmentation with the Mask frozen-DETR baseline. We visualize the predicted probability maps and the color indicates the confidence scores: red for high and blue for low.

in the following discussions. We conduct all the following ablation experiments by freezing the entire object detection network and only fine-tuning the additional introduced parameters for ~ 6 epochs on COCO instance segmentation task.

Experiment Setup. We use AdamW optimizer with an initial learning rate 1.5×10^{-4} , $\beta_1 = 0.9$, $\beta_2 = 0.999$ and a weight decay of 5×10^{-5} is employed. We train the models for 88, 500 iterations (i.e. 6 epochs), and divide the learning rate by 10 at 0.9 and 0.95 fractions of the total number of the training iterations. We follow the data pre-processing scheme of Deformable DETR [36]. We set the batch size as 8 and run all experiments with V100 GPUs with 16GB memory. We report a set of COCO metrics including AP, AP_{50} , AP_{75} , AP_S , AP_M and AP_L .

3.2. Image Feature Encoder

We first study how to improve the previous baseline setting by introducing a trainable image feature encoder to transform the image feature maps into a more suitable feature space for instance segmentation tasks. Figure 5 shows the overall pipeline. We apply the image feature encoder on feature map \mathbf{E} from the Transformer encoder. We simply modify Equation 1 as follows:

$$\mathbf{F} = \mathbf{C}_1 + \text{interpolate}(\mathcal{F}_e(\mathbf{E})), \quad (5)$$

where the $\mathcal{F}_e(\cdot)$ represents the image feature encoder that refines the image feature map for all object queries simultaneously. We study the following three kinds of modern convolution or transformer blocks.

Deformable encoder block [36]. We follow the multi-scale deformable encoder design and stack multiple multi-scale deformable encoder blocks to enhance the multi-scale feature map \mathbf{E} following:

$$\begin{aligned} \mathbf{E} &= [\mathbf{E}_1, \mathbf{E}_2, \mathbf{E}_3, \mathbf{E}_4], \\ \mathcal{F}_e(\mathbf{E}) &= \text{MultiScaleDeformableEnc}([\mathbf{E}_1, \mathbf{E}_2, \mathbf{E}_3, \mathbf{E}_4]), \end{aligned} \quad (6)$$

where $\mathbf{E}_1, \mathbf{E}_2, \mathbf{E}_3$, and \mathbf{E}_4 represent the feature maps of different scales from the Transformer encoder of the object detection system. Each multi-scale deformable encoder block

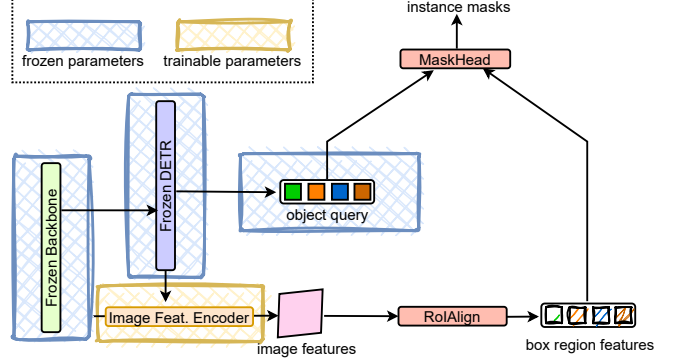


Figure 5: Add image feature encoder to Mask Frozen-DETR. We insert an additional image feature encoder to enhance the image feature maps.

block type	# layers	#FLOPs▲	#params▲	AP^{mask}	AP_{50}^{mask}	AP_{75}^{mask}	AP_S^{mask}	AP_M^{mask}	AP_L^{mask}
None	0	0.54 G	0.0 M	5.1	17.0	1.5	3.2	4.9	8.4
deformable.	1	14.71 G	0.76 M	30.8	58.2	29.5	13.5	32.7	49.0
deformable.	2	28.88 G	1.51 M	32.9	60.0	32.4	14.9	35.3	52.1
deformable.	3	43.04 G	2.27 M	33.7	60.5	33.7	15.1	36.3	53.4
Swin Trans.	1	14.20 G	0.80 M	30.0	58.0	28.0	13.8	32.3	46.3
Swin Trans.	2	27.86 G	1.59 M	31.6	59.2	30.4	14.5	34.2	48.6
Swin Trans.	3	41.51 G	2.39 M	32.2	59.6	31.3	14.9	34.8	49.5
ConvNext.	1	8.12 G	0.54 M	27.5	55.9	24.4	12.7	29.8	42.1
ConvNext.	2	15.70 G	1.08 M	30.0	58.1	27.8	13.9	32.4	46.0
ConvNext.	3	23.27 G	1.62 M	30.7	58.5	28.9	14.3	33.2	46.9

Table 2: Effect of image feature encoder design.

is implemented with $\text{MSDeformAttn} \rightarrow \text{LayerNorm} \rightarrow \text{FFN} \rightarrow \text{LayerNorm}$. FFN is implemented as $\text{Linear} \rightarrow \text{GELU} \rightarrow \text{Linear}$ by default.

Swin Transformer encoder block [21] We follow the Swin Transformer to apply a stack of multiple Swin Transformer blocks on the feature map \mathbf{E}_1 with highest resolution as follows:

$$\mathcal{F}_e(\mathbf{E}_1) = \text{SwinTransformerEnc}(\mathbf{E}_1), \quad (7)$$

where each Swin Transformer block is implemented as $\text{LayerNorm} \rightarrow \text{W-MSA} \rightarrow \text{LayerNorm} \rightarrow \text{FFN}$. W-MSA represents the window multi-head self-attention operation. We apply shifted W-MSA in the successive block to propagate information across windows following [21].

ConvNext encoder block [22] We follow the ConvNext to apply the proposed combination of large-kernel convolution and inverted bottleneck on the Transformer encoder feature map \mathbf{E}_1 following:

$$\mathcal{F}_e(\mathbf{E}_1) = \text{ConvNextBlock}(\mathbf{E}_1). \quad (8)$$

where each ConvNext block is implemented as $\text{DWC} \rightarrow \text{LayerNorm} \rightarrow \text{FFN}$. DWC represents a depth-wise convolution with large kernel size, i.e., 7×7 .

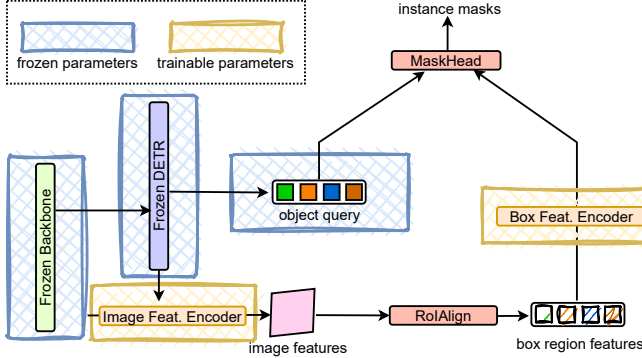


Figure 6: Add box feature encoder to Mask Frozen-DETR. We insert a feature encoder to enhance the bounding box region features.

Results. In Table 2, we compare different choices of the image feature encoder architecture design. We observe that: (i) All three image feature encoder implementations improve the instance segmentation performance. (ii) More image feature encoder layers leads to better performance, e.g., $3\times$ deformable encoder layers: $AP=32.9\%$ vs. $1\times$ deformable encoder layer: $AP=30.8\%$. (iii) Under similar computation budget, Deformable encoder block performs better, e.g., $2\times$ deformable encoder layers: $AP=32.9\%/FLOPs=28.88G$ vs. $2\times$ Swin transformer encoder layers: $AP=31.6\%/FLOPs=27.86G$ vs. $3\times$ ConvNext encoder layers: $AP=30.7\%/FLOPs=23.27G$. We use $2\times$ deformable encoder layers as the image feature encoder in the following experiments as it has a better trade-off between performance and computational cost.

3.3. Box Feature Encoder

Now we study the influence of improving the box region features with an additional box feature encoder design. We illustrate the modification in Figure 6. we simply apply additional transformation \mathcal{F}_b on \mathbf{R}_i before Equation 4 following:

$$\mathbf{R}_i = \mathcal{F}_b(\mathbf{R}_i), \quad (9)$$

where we study different choices of the box feature encoder implementation following the study on the image feature encoder design.

Channel mapper. To build an efficient box feature encoder, we propose to use a channel mapper as a simple Linear layer to decrease the channel dimension of $\mathbf{F} \in \mathbb{R}^{\frac{HW}{16} \times d}$ and apply the box region feature encoder on the updated feature map with smaller channels.

Results. We compare the effect of box feature encoder architecture design in Table 3. We notice significant computational cost increase for all settings, mainly due to two reasons: (i) the large number of bounding box region features, i.e., 100 box predictions during inference; and (ii)

block type	# layers	#FLOPs \blacktriangle	#params \blacktriangle	AP^{mask}	AP_{50}^{mask}	AP_{75}^{mask}	AP_S^{mask}	AP_M^{mask}	AP_L^{mask}
None	0	28.88 G	1.51 M	32.9	60.0	32.4	14.9	35.3	52.1
deformable.	1	98.55 G	2.46 M	44.4	67.6	48.0	24.5	47.7	62.8
deformable.	2	168.23 G	3.14 M	44.9	67.7	48.6	24.9	48.2	63.4
deformable.	3	237.91 G	3.82 M	45.1	67.8	48.9	25.2	48.4	63.7
Swin Trans.	1	112.84 G	2.31 M	42.5	66.3	45.4	23.0	45.5	61.2
Swin Trans.	2	196.81 G	3.10 M	43.7	66.9	46.8	23.8	46.8	62.3
Swin Trans.	3	280.77 G	3.89 M	44.3	67.3	47.6	24.4	47.6	62.8
ConvNext.	1	83.90 G	2.05 M	40.9	65.8	43.4	21.4	43.8	59.9
ConvNext.	2	138.92 G	2.59 M	43.0	66.9	46.0	23.4	46.1	61.7
ConvNext.	3	193.95 G	3.13 M	43.7	67.2	47.1	23.9	47.0	62.1

Table 3: Effect of box feature encoder design.

# hidden dim.	#FLOPs \blacktriangle	#params \blacktriangle	AP^{mask}	AP_{50}^{mask}	AP_{75}^{mask}	AP_S^{mask}	AP_M^{mask}	AP_L^{mask}
256	168.23 G	3.14 M	44.9	67.7	48.6	24.9	48.2	63.4
128	66.60 G	2.07 M	44.7	67.6	48.2	24.8	48.1	63.2
96	50.76 G	1.87 M	44.6	67.5	48.2	24.7	47.9	63.2
64	39.11 G	1.71 M	44.5	67.5	48.0	24.7	47.9	63.0

Table 4: Effect of hidden dimension after channel mapper.

the high-resolution of the bounding box feature map, i.e., 32×32 . We study the impact of different resolutions of the region feature maps in the ablation experiments. We find similar conclusions as Table 2: all methods improve the performance, more encoder layers lead to better performance, and deformable encoder block performs the best. Therefore, we use deformable encoder blocks for the box feature encoder. To reduce the expensive computational cost, we use the channel mapper to decrease the hidden dimension. The results are in Table 4. We observe that lower hidden dimension reduces computational cost with little performance loss. Considering the trade-off between performance and overhead, we use 128 hidden dimensions for subsequent experiments.

3.4. Query Feature Encoder

After studying the influence of adding the image feature encoder and box region feature encoder, we further investigate how to design a suitable query feature encoder to refine the object queries originally designed for detecting the boxes for instance segmentation tasks.

Object-to-object attention. The proximity of objects to each other may results in a situation where multiple instances lie within one bounding box. We add object-to-object attention to help object query representations distinguish instances. Specifically, we use multi-head self-attention mechanism to process the queries as follows:

$$[\mathbf{q}_1, \mathbf{q}_2, \dots, \mathbf{q}_N] = \text{SelfAttention}([\mathbf{q}_1, \mathbf{q}_2, \dots, \mathbf{q}_N]). \quad (10)$$

Box-to-object attention. In the frozen DETR-based object detector, the object queries are used to perform object detection and process the whole image feature instead of a box region feature. The discrepancies between the usage

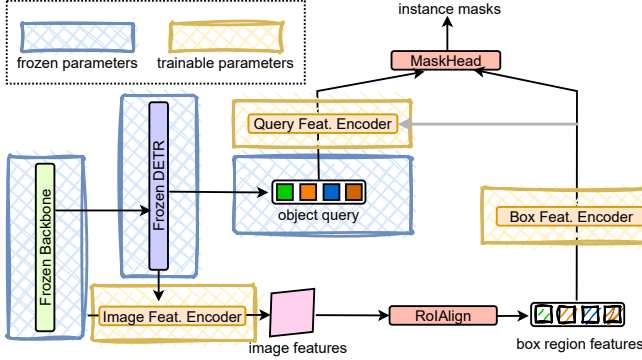


Figure 7: Add object query encoder to Frozen DETR. We apply a query feature encoder to enhance the object query representations. This is the complete framework of our Mask Frozen-DETR.

of object queries in the frozen detector and MaskHead may lead to sub-optimal segmentation results. Therefore, we introduce box-to-object attention to transform the queries and adapt them to the segmentation task as follows:

$$\mathbf{q}_i = \text{CrossAttention}(\mathbf{q}_i, \mathbf{R}_i), \quad (11)$$

where the object queries are updated by referring to the information in the box region feature.

FFN. The feed forward network (FFN) block is a widely employed element in Transformers. It is usually integrated after an attention layer to transform individual tokens. In Table 5, we investigate the efficacy of this block in adjusting object query representations for segmentation.

Results. Table 5 shows the comparison results on the effect of different modifications to the query feature encoder architecture design. We find no performance improvement when only using FFN to enhance the object queries and a minor gain (+0.1) when only using the box-to-object attention module. We think this is because the enhanced box features are already strong for instance segmentation, so using the original object query representation from the frozen detection model is enough. Moreover, using object-to-object attention reduces the performance, as the interaction between object queries might mix the semantic information of different objects. In general, we conclude that transforming the object queries is unnecessary and simply using the original ones to interact with the refined box region features achieves strong results. We only adopt the box-to-object attention design in the qualitative analysis experiments.

3.5. Other Improvements

Mask loss on sampled pixel points. Inspired by implicit PointRend [8] that shows a segmentation model can be trained with its mask loss computed on N sampled points instead of the entire mask, we compute the mask loss with

FFN	O2O	B2O	#FLOPs▲	#params▲	AP _{mask}	AP ₅₀ ^{mask}	AP ₇₅ ^{mask}	AP _S ^{mask}	AP _M ^{mask}	AP _L ^{mask}
✗	✗	✗	66.60 G	2.07 M	44.7	67.6	48.2	24.8	48.1	63.2
✓	✗	✗	66.63 G	2.33 M	44.7	67.6	48.3	24.9	48.0	63.2
✓	✓	✗	66.65 G	2.53 M	43.9	67.1	47.3	24.4	47.3	61.8
✓	✗	✓	73.40 G	2.46 M	44.8	67.6	48.4	24.9	48.1	63.4

Table 5: Effect of each factor within the query feature encoder. O2O: object-to-object attention module. B2O: box-to-object attention module.

neck	samp. sup.	pixel	mask scoring	#FLOPs▲	#params▲	AP _{mask}	AP ₅₀ ^{mask}	AP ₇₅ ^{mask}	AP _S ^{mask}	AP _M ^{mask}	AP _L ^{mask}
✗	✗	✗	✗	73.40 G	2.46 M	44.8	67.6	48.4	24.9	48.1	63.4
✓	✗	✗	✗	77.07 G	2.53 M	45.2	67.8	48.9	25.3	48.5	63.8
✓	✓	✗	✗	77.07 G	2.53 M	45.3	67.8	49.2	25.4	48.6	64.1
✓	✓	✓	✓	82.09 G	3.26 M	45.7	67.5	49.8	25.6	48.9	64.1

Table 6: Effect of other improvements including sampled pixel supervision, mask scoring, and neck design.

sampled points in the the final loss calculation. Specifically, given number of points N , oversample ratio k ($k > 1$) and importance sample ratio β ($\beta \in [0, 1]$), we randomly sample kN points from the output mask and select βN most uncertain points from the sampled points. Then we randomly sample other $(1 - \beta)N$ points from the output mask and compute loss only on these N points.

Mask scoring. Since the classification scores predicted by the frozen DETR cannot reflect the quality of segmentation masks, we introduce mask scoring [16] to our method to adjust the score, making it able to describe the quality of segmentation masks more precisely. Specifically, the mask scoring head takes the output mask and box region features as input and uses them to predict the iou score between the output mask and ground truth following:

$$\text{iou}_i = \text{MLP}(\text{Flatten}(\text{Conv}(\text{Cat}(\mathbf{M}_i, \mathbf{R}_i)))), \quad (12)$$

where Cat, Conv and MLP refer to concatenation, convolution layers and multi layer perceptron, respectively. The iou score predicted by the mask scoring head is then used to adjust the classification score as following:

$$s_i = c_i \text{iou}_i, \quad (13)$$

where s_i is the confidence score of the output mask.

Neck for backbone feature. The feature map output by the first stage of backbone $\mathbf{C}_1 \in \mathbb{R}^{\frac{HW}{16} \times d}$ may not contain sufficient semantic information for accurate instance segmentation. Therefore, we introduce a simple neck block to encode more semantic information into the high resolution feature map \mathbf{C}_1 . The neck block can be described using the following formula:

$$\mathbf{C}_1 = \text{GN}(\text{PWConv}(\mathbf{C}_1)), \quad (14)$$

where GN and PWConv refer to group normalization and point-wise convolution, respectively.

method	backbone	#epochs	Object365	AP ^{box}	AP ^{mask}	AP ^{mask} ₅₀	AP ^{mask} ₇₅	AP ^{mask} _S	AP ^{mask} _M	AP ^{mask} _L	GPU Hours
K-Net-N256 [35]	R50	36	✗	–	38.6	60.9	41.0	19.1	42.0	57.7	–
QueryInst [11]	Swin-L	50	✗	56.1	48.9	74.0	53.9	30.8	52.6	68.3	–
Mask2Former [6]	R50	50	✗	–	43.7	–	–	23.4	47.2	64.8	502
Mask2Former [6]	Swin-L	100	✗	–	50.1	–	–	29.9	53.9	72.1	1,700
Mask DINO [18]	R50	50	✗	50.5	46.0	68.9	50.3	26.0	49.3	65.5	1,404
Mask DINO [18]	Swin-L	50	✗	58.3	52.1	76.5	57.6	32.9	55.4	72.5	2,400
Mask Frozen- \mathcal{H} -DETR	R50	6	✗	49.9	44.1	66.2	47.8	24.4	47.0	62.6	49
Mask Frozen- \mathcal{H} -DETR	Swin-L	6	✗	59.1	51.9	75.8	57.2	31.6	55.1	71.6	179
ViT-Adapter-L [5]	ViT-L	8	✓	61.8	53.0	–	–	–	–	–	1,068
Mask DINO [18]	Swin-L	24	✓	–	54.5	–	–	–	–	–	1,600
Mask Frozen- \mathcal{H} -DETR	R50	6	✓	52.2	45.7	67.5	49.8	25.6	48.9	64.1	49
Mask Frozen- \mathcal{H} -DETR	Swin-L	6	✓	62.3	54.0	77.9	59.5	35.6	57.4	73.0	172
Mask Frozen-DINO-DETR	FocalNet-L	6	✓	63.2	54.9	78.9	60.8	37.2	58.4	72.9	136

Table 7: Comparison with SOTA instance segmentation methods on COCO val.

method	backbone	#epochs	Object365	AP ^{box}	AP ^{mask}	AP ^{mask} ₅₀	AP ^{mask} ₇₅	AP ^{mask} _S	AP ^{mask} _M	AP ^{mask} _L
K-Net-N256 [35]	R101	36	✗	–	40.6	63.3	43.7	18.8	43.3	59.0
SOLQ [10]	Swin-L	50	✗	56.5	46.7	–	–	29.2	50.1	60.9
SOIT [33]	Swin-L	36	✗	56.9	49.2	74.3	53.5	30.2	52.7	65.2
QueryInst [11]	Swin-L	50	✗	56.1	49.1	74.2	53.8	31.5	51.8	63.2
Mask2Former [6]	Swin-L	100	✗	–	50.5	74.9	54.9	29.1	53.8	71.2
Mask DINO [18]	Swin-L	24	✓	–	54.7	–	–	–	–	–
Mask Frozen-DINO-DETR	FocalNet-L	6	✓	63.2	55.3	79.3	61.4	37.8	58.4	70.4

Table 8: Comparison with SOTA instance segmentation methods on COCO test-dev.

Results. In Table 6, we attempt to further improve the results by integrating a neck block design, using sampled pixel supervision, and using mask scoring. We observe that all three designs bring consistent gains in AP scores. For example, using the neck block improves AP from 44.8% to 45.2% and using mask scoring improves AP from 45.3% to 45.7%. Notably, while sampled pixel supervision reduces the number of the points for training supervisions by 75%, it still brings a slight gain in AP (+0.1%). Therefore, we use all three designs in the following experiments.

4. Comparison with SOTA Systems

To compare our system with state-of-the-art instance segmentation methods, we construct a series of strong Mask Frozen-DETR models based on different Frozen DETR-based detector weights. These include Mask Frozen- \mathcal{H} -DETR + ResNet-50, which uses \mathcal{H} -DETR + ResNet-50 with AP^{box} of 52.2%; Mask Frozen- \mathcal{H} -DETR + Swin-L, which uses \mathcal{H} -DETR + Swin-L with AP^{box} of 62.3%; and Mask Frozen-DINO-DETR + Swin-L, which uses DINO-DETR + FocalNet-L with AP^{box} of 63.2%.

Table 7 presents the detailed comparison results on COCO val set. We can see that, with Object365 object detection pre-training, our approach surpasses the very recent state-of-the-art Mask-DINO by a clear margin (ours: 54.9% vs. Mask DINO: 54.5%). This result is remarkable consid-

ering that the strong object detector DINO-DETR achieves even better object detection performance, i.e., 63.2%, than the DINO-DETR + FocalNet-L that we use. The most important advantage of our approach is the significantly reduced training time, e.g., we can complete the training of DINO-DETR + FocalNet-L within 17× **hours** while training a Mask DINO + Swin-L takes more than 8× **days** when using 8× V100 GPUs.

We also provide the detailed comparison results for Mask Frozen- \mathcal{H} -DETR + ResNet-50 and Mask Frozen- \mathcal{H} -DETR + Swin-L. In general, our approach achieves competitive results across various model sizes and different DETR-based frameworks. We further compare Mask Frozen-DINO-DETR to the state-of-the-art methods in instance segmentation on COCO test-dev in Table 8. Frozen-DINO-DETR with FocalNet-L achieves an AP of 55.3%. This result surpasses the recent state-of-the-art method, Mask DINO, by +0.6 AP.

5. Ablation Experiments and Analysis

RoIAlign output size. Table 9 shows the the influence of RoIAlign output size. We observe that (i) Enlarging the RoIAlign output size significantly increases GFLOPs. (ii) Increasing RoIAlign output size can improve instance segmentation performance. Specifically, we observe a 0.9 improvement in AP by increasing the output size from 16 × 16

output size	#FLOPs▲	#params▲	AP ^{mask}	AP ^{mask} ₅₀	AP ^{mask} ₇₅	AP ^{mask} _S	AP ^{mask} _M	AP ^{mask} _L
16 × 16	46.09 G	2.97 M	44.8	67.5	49.1	25.4	48.0	62.0
32 × 32	82.09 G	3.26 M	45.7	67.5	49.8	25.6	48.9	64.1
64 × 64	225.86 G	4.44 M	45.9	67.6	50.2	25.8	49.1	64.4

Table 9: Effect of RoIAlign output size.

epoch	AP ^{mask}	AP ^{mask} ₅₀	AP ^{mask} ₇₅	AP ^{mask} _S	AP ^{mask} _M	AP ^{mask} _L
6	45.7	67.5	49.8	25.6	48.9	64.1
12	46.0	67.7	50.3	25.9	49.1	64.3

Table 10: Effect of training epochs.

LSJ	GPU Hour	AP ^{mask}	AP ^{mask} ₅₀	AP ^{mask} ₇₅	AP ^{mask} _S	AP ^{mask} _M	AP ^{mask} _L
✗	49	45.7	67.5	49.8	25.6	48.9	64.1
✓	63	46.0	67.7	50.1	26.1	49.1	64.0

Table 11: Effect of large scale jittering.

mask head	#FLOPs▲	#params▲	AP ^{mask}	AP ^{mask} ₅₀	AP ^{mask} ₇₅	AP ^{mask} _S	AP ^{mask} _M	AP ^{mask} _L
dot product	82.09 G	3.26 M	45.7	67.5	49.8	25.6	48.9	64.1
segmenter head	83.77 G	3.29 M	45.7	67.6	49.9	25.6	48.9	64.1

Table 12: Effect of instance mask head design.

batch size	AP ^{mask}	AP ^{mask} ₅₀	AP ^{mask} ₇₅	AP ^{mask} _S	AP ^{mask} _M	AP ^{mask} _L
2	45.9	67.7	50.0	25.7	49.0	64.2
4	45.9	67.6	49.9	25.8	49.0	64.3
8	45.7	67.5	49.8	25.6	48.9	64.1

Table 13: Effect of batch size.

to 32×32 . (iii) Instance segmentation performance saturates beyond an RoIAlign output size of 32×32 . Taking into account the trade-off between performance and computational cost, we set RoIAlign output size as 32×32 by default.

Training epochs. Table 10 shows the effect of training epochs. We notice that doubling the number of training epochs only brings 0.3 gain in AP. This result suggests that our model achieves convergence promptly, which can effectively reduce the required training time.

Large scale jittering. Table 11 shows the effect of large scale jittering. We observe that using large scale jittering achieves a 0.3 AP improvement and increase the training GPU hours by 28.6%. In light of the trade-off between training time and performance, we do not utilize large scale jittering in our following experiments.

Instance mask head design. We compare the effect of mask head design in Table 12. Compared with segmenter head [28] that contains linear projection and normalization, our simple dot product design achieves comparable AP scores with lower FLOPs and fewer number of parameters.

Batch size. Table 13 shows the effect of batch size. We observe that reducing the batch size from 8 to 4 or 2 even

layer#	AP ^{mask}	AP ^{mask} ₅₀	AP ^{mask} ₇₅	AP ^{mask} _S	AP ^{mask} _M	AP ^{mask} _L
2	45.7	67.5	49.8	25.7	48.9	64.0
4	45.7	67.5	49.8	25.6	48.9	64.1
6	45.5	67.5	49.3	25.6	48.7	63.7

Table 14: Layer index of the encoder feature map **E**.

brings slightly improvements in performance (+0.2 AP). It is worth noting that our method can run on a single V100 GPU with 16G memory when the batch size is 2. This highlights the effectiveness and computational resource efficiency of our approach.

Layer index of the encoder feature map. We compare the encoder feature map **E** from different layers of the Transformer encoder in Table 14. We notice that using the encoder feature map from shallower layers outperforms using that from the last layer of the encoder. We think this is because the feature map from the last layer of the encoder contains task-specific information relevant to detection, while feature maps from shallower layers contain more generalized object information that may facilitate segmentation. Therefore, we use the encoder feature map from layer#4 by default.

Effect of the depth of the image feature encoder and the box feature encoder Table 15 shows the influence of the depth of image feature encoder and the box feature encoder on Mask Frozen-DINO-DETR with FocalNet-L as backbone. We observe that: (i) The instance segmentation performance of Frozen-DINO-DETR reaches saturation when the depth of the box feature encoder is 2, and further increasing its depth does not result in a performance gain. (ii) Increasing the depth of image feature encoder from 2 to 3 leads to a 0.1 increase in AP. Nevertheless, the performance saturates when the depth of image feature encoder is 3. Given these findings, we select the depth of the image feature encoder to be 3 and the depth of the box feature encoder to be 2 for the comparisons with state-of-the-art instance segmentation methods on the COCO test-dev.

Effect of fine-tuning DETR: We further ablate the effect of fine-tuning the DETR-based object detector either entirely or partially, as outlined in Table 16. Accordingly, we observe that (i) fine-tuning DETR brings consistent, albeit marginal, gains while significantly increasing the overall training GPU hours; (ii) our method achieves the best trade-off between performance and training cost.

Qualitative results. Figure 8 shows the instance segmentation probability maps based on our approach. We notice that the probability maps precisely capture the object boundaries, which support the strong performance of our approach on instance segmentation tasks.

# img. enc. layers	# box enc. layers	#FLOPs▲	#params▲	AP ^{mask}	AP ^{mask} ₅₀	AP ^{mask} ₇₅	AP ^{mask} _S	AP ^{mask} _M	AP ^{mask} _L
2	2	262.27 G	3.24 M	54.9	78.9	60.8	37.2	58.4	72.9
2	3	326.65 G	3.62 M	54.9	78.9	60.7	37.0	58.5	72.9
3	2	320.44 G	4.03 M	55.0	78.9	60.9	37.1	58.5	73.0
3	3	384.82 G	4.40 M	55.0	78.9	60.9	37.2	58.5	73.1
4	4	507.38 G	5.56 M	55.0	78.9	60.8	37.2	58.4	73.2

Table 15: Effect of the depth of the image feature encoder and the box feature encoder on DINO + FocalNet-L.

detector method	image feat. enc.	box feat. enc.	query feat. enc.	partial finetune	finetune	AP ^{mask}	GPU Hours
H-DETR+R50	✓	✓	✓	✗	✗	45.7	49
	✗	✗	✗	✓	✗	43.8	92
	✗	✗	✗	✗	✓	43.9	99
	✓	✓	✓	✓	✗	45.6	100
	✓	✓	✓	✗	✓	46.0	108
H-DETR+Swin-L	✓	✓	✓	✗	✗	54.0	172
	✓	✓	✓	✓	✗	54.1	406
	✓	✓	✓	✗	✓	54.1	532
DINO-DETR+FocalNet	✓	✓	✓	✗	✗	54.9	136
	✓	✓	✓	✓	✗	54.9	218
	✓	✓	✓	✗	✓	55.0	319

Table 16: Effect of fine-tuning the whole DETR (fine-tune) or only the transformer encoder & decoder within DETR (partial fine-tune). During fine-tuning, we set the learning rate of the original DETR parameters as 1/10 of the ones of the additional new parameters.

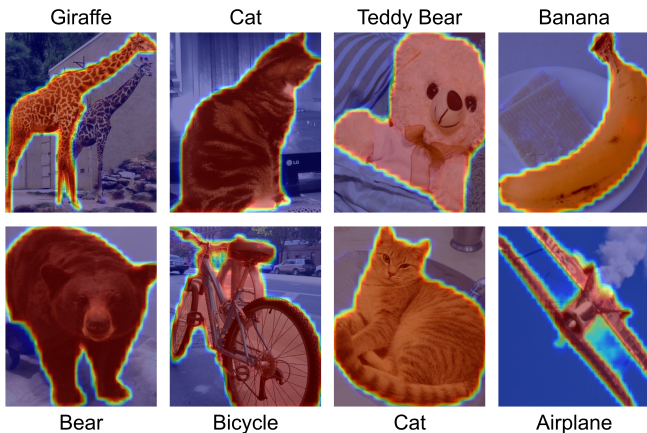


Figure 8: Visualizing the segmentation probability maps of our approach.

6. Conclusion

In this work, we have presented the detailed techniques for converting an existing off-the-shelf DETR-based object detector into a strong instance segmentation model with minimal training time and resources. Our approach is remarkably simple yet effective. We verify the effectiveness of our approach by reporting state-of-the-art instance segmentation results while accelerating the training by more than $10\times$ times. We believe our simple approach can inspire more research on advancing the state-of-the-art in instance segmentation model design.

References

- [1] Z. Cai and N. Vasconcelos. Cascade r-cnn: Delving into high quality object detection. In *CVPR*, pages 6154–6162, 2018. 1, 2
- [2] Z. Cai and N. Vasconcelos. Cascade r-cnn: high quality object detection and instance segmentation. *IEEE transactions on pattern analysis and machine intelligence*, 43(5):1483–1498, 2019. 1
- [3] N. Carion, F. Massa, G. Synnaeve, N. Usunier, A. Kirillov, and S. Zagoruyko. End-to-end object detection with transformers. In *European conference on computer vision*, pages 213–229. Springer, 2020. 2
- [4] K. Chen, J. Pang, J. Wang, Y. Xiong, X. Li, S. Sun, W. Feng, Z. Liu, J. Shi, W. Ouyang, et al. Hybrid task cascade for instance segmentation. In *CVPR*, pages 4974–4983, 2019. 2
- [5] Z. Chen, Y. Duan, W. Wang, J. He, T. Lu, J. Dai, and Y. Qiao. Vision transformer adapter for dense predictions. *arXiv preprint arXiv:2205.08534*, 2022. 7
- [6] B. Cheng, I. Misra, A. G. Schwing, A. Kirillov, and R. Girshar. Masked-attention mask transformer for universal image segmentation. *arXiv preprint arXiv:2112.01527*, 2021. 7
- [7] B. Cheng, I. Misra, A. G. Schwing, A. Kirillov, and R. Girshar. Masked-attention mask transformer for universal image segmentation. In *Proceedings of the IEEE/CVF Conference on Computer Vision and Pattern Recognition*, pages 1290–1299, 2022. 1, 2
- [8] B. Cheng, O. Parkhi, and A. Kirillov. Pointly-supervised instance segmentation. In *Proceedings of the IEEE/CVF Conference on Computer Vision and Pattern Recognition*, pages 2617–2626, 2022. 6
- [9] B. Cheng, A. Schwing, and A. Kirillov. Per-pixel classification is not all you need for semantic segmentation. *Advances in Neural Information Processing Systems*, 34, 2021. 2
- [10] B. Dong, F. Zeng, T. Wang, X. Zhang, and Y. Wei. Solq: Segmenting objects by learning queries. *NeurIPS*, 2021. 7
- [11] Y. Fang, S. Yang, X. Wang, Y. Li, C. Fang, Y. Shan, B. Feng, and W. Liu. Instances as queries. In *ICCV*, pages 6910–6919, October 2021. 2, 7
- [12] R. Girshick, J. Donahue, T. Darrell, and J. Malik. Rich feature hierarchies for accurate object detection and semantic segmentation. In *Proceedings of the IEEE conference on computer vision and pattern recognition*, pages 580–587, 2014. 2
- [13] H. He, Y. Yuan, X. Yue, and H. Hu. Rankseg: Adaptive pixel classification with image category ranking for segmentation. In *European Conference on Computer Vision*, pages 682–700. Springer, 2022. 2

- [14] K. He, G. Gkioxari, P. Dollár, and R. Girshick. Mask R-CNN. In *ICCV*, 2017. 2, 3
- [15] K. He, X. Zhang, S. Ren, and J. Sun. Deep Residual Learning for Image Recognition. In *CVPR*, 2016. 1
- [16] Z. Huang, L. Huang, Y. Gong, C. Huang, and X. Wang. Mask scoring r-cnn. In *Proceedings of the IEEE/CVF conference on computer vision and pattern recognition*, pages 6409–6418, 2019. 6
- [17] D. Jia, Y. Yuan, H. He, X. Wu, H. Yu, W. Lin, L. Sun, C. Zhang, and H. Hu. Detr with hybrid matching. *arXiv preprint arXiv:2207.13080*, 2022. 1, 2
- [18] F. Li, H. Zhang, S. Liu, L. Zhang, L. M. Ni, H.-Y. Shum, et al. Mask dino: Towards a unified transformer-based framework for object detection and segmentation. *arXiv preprint arXiv:2206.02777*, 2022. 1, 2, 7
- [19] W. Liang, Y. Yuan, H. Ding, X. Luo, W. Lin, D. Jia, Z. Zhang, C. Zhang, and H. Hu. Expediting large-scale vision transformer for dense prediction without fine-tuning. *Advances in Neural Information Processing Systems*, 2022. 2
- [20] Y. Lin, Y. Yuan, Z. Zhang, C. Li, N. Zheng, and H. Hu. Detr doesn’t need multi-scale or locality design, 2023. 2
- [21] Z. Liu, Y. Lin, Y. Cao, H. Hu, Y. Wei, Z. Zhang, S. Lin, and B. Guo. Swin transformer: Hierarchical vision transformer using shifted windows. In *ICCV*, pages 10012–10022, 2021. 1, 4
- [22] Z. Liu, H. Mao, C.-Y. Wu, C. Feichtenhofer, T. Darrell, and S. Xie. A convnet for the 2020s. In *Proceedings of the IEEE/CVF Conference on Computer Vision and Pattern Recognition*, pages 11976–11986, 2022. 4
- [23] Y. Ma, W. Liang, Y. Hao, B. Chen, X. Yue, C. Zhang, and Y. Yuan. Revisiting detr pre-training for object detection. *arXiv preprint arXiv:2308.01300*, 2023. 2
- [24] J. Redmon, S. Divvala, R. Girshick, and A. Farhadi. You only look once: Unified, real-time object detection. In *Proceedings of the IEEE conference on computer vision and pattern recognition*, pages 779–788, 2016. 2
- [25] S. Ren, K. He, R. Girshick, and J. Sun. Faster r-cnn: Towards real-time object detection with region proposal networks. *Advances in neural information processing systems*, 28, 2015. 2
- [26] J. Schult, F. Engelmann, A. Hermans, O. Litany, S. Tang, and B. Leibe. Mask3d for 3d semantic instance segmentation. *arXiv preprint arXiv:2210.03105*, 2022. 2
- [27] S. Shao, Z. Li, T. Zhang, C. Peng, G. Yu, X. Zhang, J. Li, and J. Sun. Objects365: A large-scale, high-quality dataset for object detection. In *ICCV*, pages 8430–8439, 2019. 3
- [28] R. Strudel, R. Garcia, I. Laptev, and C. Schmid. Segmenter: Transformer for semantic segmentation. *arXiv preprint arXiv:2105.05633*, 2021. 8
- [29] J. Sun, C. Qing, J. Tan, and X. Xu. Superpoint transformer for 3d scene instance segmentation. *arXiv preprint arXiv:2211.15766*, 2022. 2
- [30] P. Sun, R. Zhang, Y. Jiang, T. Kong, C. Xu, W. Zhan, M. Tomizuka, L. Li, Z. Yuan, C. Wang, et al. Sparse r-cnn: End-to-end object detection with learnable proposals. In *Proceedings of the IEEE/CVF conference on computer vision and pattern recognition*, pages 14454–14463, 2021. 2
- [31] W. Wang, J. Dai, Z. Chen, Z. Huang, Z. Li, X. Zhu, X. Hu, T. Lu, L. Lu, H. Li, et al. Internimage: Exploring large-scale vision foundation models with deformable convolutions. *arXiv preprint arXiv:2211.05778*, 2022. 2
- [32] X. Wang, R. Zhang, T. Kong, L. Li, and C. Shen. Solov2: Dynamic and fast instance segmentation. In *NeurIPS*, 2020. 2
- [33] X. Yu, D. Shi, X. Wei, Y. Ren, T. Ye, and W. Tan. Soit: Segmenting objects with instance-aware transformers. In *AAAI*, volume 36, pages 3188–3196, 2022. 7
- [34] H. Zhang, F. Li, S. Liu, L. Zhang, H. Su, J. Zhu, L. M. Ni, and H.-Y. Shum. Dino: Detr with improved denoising anchor boxes for end-to-end object detection. *arXiv preprint arXiv:2203.03605*, 2022. 1, 2
- [35] W. Zhang, J. Pang, K. Chen, and C. C. Loy. K-net: Towards unified image segmentation. *NeurIPS*, 34:10326–10338, 2021. 7
- [36] X. Zhu, W. Su, L. Lu, B. Li, X. Wang, and J. Dai. Deformable detr: Deformable transformers for end-to-end object detection. *arXiv preprint arXiv:2010.04159*, 2020. 2, 4